PAPER

Application of a non-steady-state orbit-following Monte-Carlo code to neutron modeling in the MAST spherical tokamak

To cite this article: K Tani *et al* 2016 *Plasma Phys. Control. Fusion* **58** 105005

IOP Publishing Plasma Physics and Controlled Fusion
Plasma Phys. Control. Fusion **58** (2016) 105005 (14pp) doi:10.1088/0741-3335/58/10/105005

Application of a non-steady-state orbit-following Monte-Carlo code to neutron modeling in the MAST spherical tokamak

K Tani[1], K Shinohara[2], T Oikawa[2], H Tsutsui[1], K G McClements[3], R J Akers[3], Y Q Liu[3], M Suzuki[4], S Ide[2], Y Kusama[2] and S Tsuji-Iio[1]

[1] Tokyo Institute of Technology, Ookayama Campus, 2-12-1 Ookayama, Meguro-ku, Tokyo 152-8550, Japan
[2] National Institutes for Quantum and Radiological Science and Technology, Naka, Ibaraki 311-0193, Japan
[3] CCFE, Culham Science Centre, Abingdon, Oxfordshire, OX14 3DB, UK
[4] Computer Associated Laboratory, Hitachinaka, Ibaraki 312-0045, Japan

E-mail: tani.keiji@nr.titech.ac.jp

Received 3 April 2016, revised 27 June 2016
Accepted for publication 25 July 2016
Published 31 August 2016

Abstract
As part of the verification and validation of a newly developed non-steady-state orbit-following Monte-Carlo code, application studies of time dependent neutron rates have been made for a specific shot in the Mega Amp Spherical Tokamak (MAST) using 3D fields representing vacuum resonant magnetic perturbations (RMPs) and toroidal field (TF) ripples. The time evolution of density, temperature and rotation rate in the application of the code to MAST are taken directly from experiment. The calculation results approximately agree with the experimental data. It is also found that a full orbit-following scheme is essential to reproduce the neutron rates in MAST.

Keywords: fast ions, Monte-Carlo, non-steady-state, neutron rate, MAST

(Some figures may appear in colour only in the online journal)

1. Introduction

As part of analyzing experimental data from a fusion device or designing a new device, it is common to conduct numerical simulations of fast-ion confinement. For this purpose, various orbit-following Monte-Carlo codes have been developed for the simulation of fast-ion confinement in 3D magnetic fields [1–5]. In these codes, test particles are initially generated using Monte-Carlo techniques and their trajectories are followed until they slow down via Coulomb collisions with bulk electrons and ions or are lost to the first wall in a steady state plasma and a 3D magnetic field. That is to say, these codes essentially analyze the confinement of fast ions produced by a constant source in steady-state conditions. Consequently, these codes are designed for the analysis of experimental data in a shot with a flat-top time much longer than the slowing down time of fast ions.

In a small or medium size fusion device, however, plasma parameters often evolve on timescales that are not small compared to the fast-ion slowing-down time, while in a large device, short-pulse neutral beams are sometimes injected to observe the confinement of fast ions. Recently, experiments that include the application of resonant magnetic perturbations (RMPs) produced by external magnetic coils have been conducted in many tokamaks with the aim of diminishing the heat load on divertor components caused by edge localized modes (ELMs) [6–8]. However, the RMPs can have a strong effect on the absolute values and profiles of plasma parameters, such as density and toroidal rotation velocity. The RMP field also has an important effect on the confinement of fast ions [9–12], which may also change the bulk plasma parameters.

For the time-dependent analysis of fast ions, the NUBEAM code has been widely used [13, 14]. This code, however, basically treats fast ions in an axi-symmetric field with simplified

models for the effects of non-axi-symmetric fields. In order to make more precise time-dependent analyses of fast ions, we need a tool to follow their guiding-centers or full orbits in 3D magnetic fields.

To satisfy this requirement, we have remodeled an existing steady-state orbit-following Monte-Carlo code and developed a non-steady-state version in which time dependent treatments of plasma parameters, neutral beam injection (NBI) and magnetic perturbations are available.

An outline of the non-steady-state orbit-following Monte Carlo code, hereafter simply referred to as the NSS-OFMC code, is described in section 2. As part of the verification and validation of the NSS-OFMC code, we calculated time dependent neutron rates for a typical shot in the Mega Amp Spherical Tokamak (MAST) [15]. The results are shown in section 3. Conclusions of the present work are summarized in section 4.

2. Outline of non-steady-state orbit-following Monte Carlo code

2.1. Steady-state orbit-following Monte Carlo code

A steady-state orbit-following Monte Carlo code, hereafter simply referred to as the SS OFMC code, was developed at the Japan Atomic Energy Agency (JAEA) more than 30 years ago [1]. In the SS OFMC code, fast ions are initially generated as test particles using Monte-Carlo techniques.

In the case of NBI, the code can take into account multi-beam lines, multi-beam-energy components for each beam line and a finite beam volume. When generating a test particle, a beam line and a beam-energy component are selected first by two random numbers ($\chi_{\rm NB1}$, $\chi_{\rm NB2}$) which accord with the ratios of the particle rates of the beam lines and the beam-energy components. Assuming a Gaussian radial distribution of the beam, the radial position and the azimuthal angle of the beam launching point are given by generating a Gaussian random number ($\chi_{\rm NB3}$) and a uniform random number ($\chi_{\rm NB4}$). After setting these parameters, the birth point of a fast ions is calculated by a fifth random number $\chi_{\rm NB5}$ as follows:

$$\chi_{\rm NB5} = \exp\left(-\int_0^{l^*} n_e \sigma_s {\rm d}l\right), \tag{1}$$

where n_e is the plasma density; σ_s, the total stopping cross section of the neutral beams in the plasma and l^*, the beam path length from the plasma surface to the ionization point along the beam line described above.

In the case of fast ions produced by fusion reactions [16], the initial birth flux surface and the poloidal angle of the kth test particle (ψ_k, θ_k) are given by

$$\xi_\psi = \int_0^{\psi_k} S_{\rm fusion}(\psi)\frac{{\rm d}V}{{\rm d}\psi}{\rm d}\psi \Big/ \int_0^{\psi_a} S_{\rm fusion}(\psi)\frac{{\rm d}V}{{\rm d}\psi}{\rm d}\psi, \tag{2}$$

$$\xi_\theta = \int_0^{\theta_k} \frac{{\rm d}l_\theta}{B_{\rm p}} \Big/ \oint \frac{{\rm d}l_\theta}{B_{\rm p}}, \tag{3}$$

where ξ_ψ and ξ_θ are uniform random numbers between zero and unity; $S_{\rm fusion}(\psi)$, the local fusion reaction rate; ψ_a, the poloidal flux function at the plasma edge; $B_{\rm p}$, the poloidal magnetic field; V, the plasma volume as a function of ψ; and ${\rm d}l_\theta$, the poloidal differential path length along the magnetic flux surface at $\psi = \psi_k$.

After the generation of fast-ion test particles, their guiding-center orbits or gyro-orbits (full orbits) in 3D magnetic fields are numerically followed until they are lost to the first wall or slow down to thermal energy via Coulomb collisions with bulk plasma electrons and ions. Hereafter, the terms 'guiding-center' and 'full-orbit' are simply referred to as GC and FO. Using Monte-Carlo techniques, calculations of Coulomb collisions are executed at intervals which are much shorter than the bounce time of fast ions. Details of the calculations of Coulomb collisions are described in the appendix. Finally, statistical calculations are performed to extract the physical quantities of fast ions.

During the above calculation steps, the steady-state fast-ion relevant quantities P are also calculated as follows;

$$P(\psi_i) = \int_0^{\tau_{s0}} \sum_{k(i)} p(\psi_k(t)) w_k {\rm d}t / V_i, \tag{4}$$

where p is a fast ion parameter; $\psi_k(t)$ is the normalized poloidal flux function of the kth test particle at time t; τ_{s0} the slowing down time at the plasma center; i the radial mesh number ith respect to ψ; V_i the plasma volume within the ith radial mesh; and w_k the birth rate of the kth test particle, respectively. The integration is executed simultaneously with the orbit following for each test particle. The functional symbol $\sum_{k(i)}$ in equation (1) denotes the summation of test particles which are in the ith radial mesh at time t.

If we take $p = 1.0$ and $p = E$ in equation (1), the steady-state radial distribution of fast-ion density and fast-ion pressure are obtained respectively, where E is the energy of fast ions. For the case in which deuteron (D) neutral beams are injected into a D plasma, the total neutron rate is obtained as $\sum_i P(\psi_i)$ with $p = n_{\rm D}\langle\sigma v\rangle_{\rm DD}$, where $n_{\rm D}$ is the D-ion density of bulk plasma and $\langle\sigma v\rangle_{\rm DD}$ is the D–D fusion reaction rate. For a 4D discretization with respect to $(R, Z, v, v_{//}/v)$ and $p = 1.0$, the 4D steady-state distribution of D fast-ion density $n_{\rm D}^{\rm f}(R, Z, v, v_{//}/v)$ can be estimated where R and Z are the major radius and the vertical positions, respectively; and v and $v_{//}$ are the velocity and the velocity component parallel to the magnetic field line, respectively. Using the above $n_{\rm D}^{\rm f}(R, Z, v, v_{//}/v)$ as estimated earlier, the birth rate of fusion produced tritons (Ts) can be calculated in the next step. Following the orbits of those T ions, an estimation of the D–T neutron rate becomes available with $p = n_{\rm D}\langle\sigma v\rangle_{\rm DT}$ where $\langle\sigma v\rangle_{\rm DT}$ is the D–T fusion reaction rate.

In the OFMC code, the time mesh for the calculation of Coulomb collisions $\Delta t_{\rm col}$ is set to be much longer than the orbit-following time-mesh $\Delta t_{\rm orbit}$ and much shorter than the orbit bounce time $\tau_{\rm b}$ which is much shorter than the slowing down time, that is,

$$\Delta t_{\rm orbit} \ll \Delta t_{\rm col} \ll \tau_{\rm b} \ll \tau_{\rm s0}.$$

Table 1. Distribution of plasma-relevant quantities which can be calculated with the OFMC code.

Distribution of fast-ion relavant quantities in the plasma		p	Time-integration (summation) step
1	Total fast-ion density	1.0	$\Delta t_{\rm orbit}$
2	Fast-ion pressure	E	Do
3	Canonical angular momentum	P_ϕ	Do
4	Neutron rate (D beam)	$n_{\rm D}\langle\sigma v\rangle_{\rm DD}, n_{\rm T}\langle\sigma v\rangle_{\rm DT}$	Do
5	Fast-ion (beam-droven) current[a]	$v_{//}B$	Do
6	JXB torque[b]	$e_{\rm f}/\tau_{\rm s}$	Do
7	Beam-power deposition	ΔE^β	$\Delta t_{\rm col}$
8	Collisional torque	$m_{\rm f}R\Delta v_{//}^\beta B_\phi/B$	Do

[a] : Details are in [17,18].
[b]: Details are in [19].
ΔE^β: equations (A.15) and (A.16), $\Delta v_{//}^\beta$: equation (A.17).

The OFMC code employs an equal collision time mesh which is common to all the test particles given by $\Delta t_{\rm col} = \tau_{\rm s0}/M_{\rm max}$ where $M_{\rm max}$ is usually set to be about 10^6. The radial profiles of fast-ion power density deposited to the bulk-plasma species β can be estimated through a procedure similar to equation (1), as follows:

$$P_{\rm dep}^\beta(\psi_i) = -\sum_{m=1}^{M_{max}}\sum_{k(i)}\Delta E^\beta(\psi_k(t_m))w_k/V_i, \qquad (5)$$

where ΔE^β is the energy change of the kth test particle due to Coulomb collisions (see equation (A.15) or (A.16) in appendix) at $t = t_m = m\Delta t_{\rm col}$. The radial distribution of fast-ion relevant quantities available using the OFMC code are listed in table 1.

Calculations of the charge exchange of fast ions with background neutral particles and the reionization process are also made at every $\Delta t_{\rm col}$ simultaneously with the calculations of Coulomb collisions.

The flow of the steady-state OFMC scheme is shown in figure 1.

2.2. Non-steady-state orbit-following Monte-Carlo code.

In the newly developed non-steady-state (NSS) orbit-following Monte-Carlo code, the following time dependent parameters are available:

- Plasma parameters (densities, temperatures, rotation velocities and Zeff),
- NBI parameters and
- 3D magnetic perturbations (ELM control magnetic fields and TAE modes).

The code also can vary in time the generation of fusion produced fast ions, depending on the above non-steady-state plasma parameters.

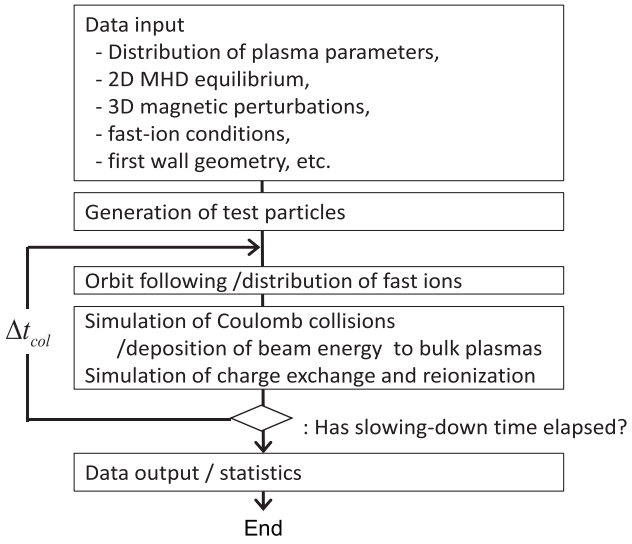

Figure 1. Flow of the steady-state OFMC scheme.

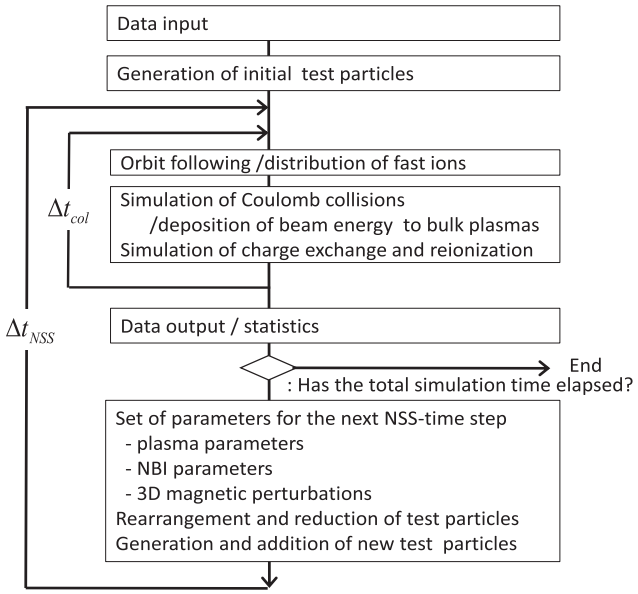

Figure 2. Flow of the non-steady-state OFMC scheme.

In the NSS scheme, a new time mesh $\Delta t_{\rm NSS}$ is set to control the non-steady-state calculations. Generally, $\Delta t_{\rm NSS}$ is set to be much longer than $\tau_{\rm b}$ and much shorter than $\tau_{\rm s0}$, that is,

$$\Delta t_{\rm orbit} \ll \Delta t_{\rm col} \ll \tau_{\rm b} \ll \Delta t_{\rm NSS} \ll \tau_{\rm s0}.$$

Typically,

$$\Delta t_{\rm NSS} = \tau_{\rm s0}/N_{\rm NSS},$$

with $N_{\rm NSS} \approx 100$. All of the above parameters are expected to change slowly, such that they are approximately constant during the short time interval $\Delta t_{\rm NSS}$.

The flow of the non-steady-state OFMC scheme is shown in figure 2. As shown in figures 1 and 2, the main loops which consist of the orbit following, the simulation of Coulomb collisions and the simulation of charge-exchange/reionization in both the SS and NSS schemes are basically the same. While the main loop in the SS scheme is executed for all initially

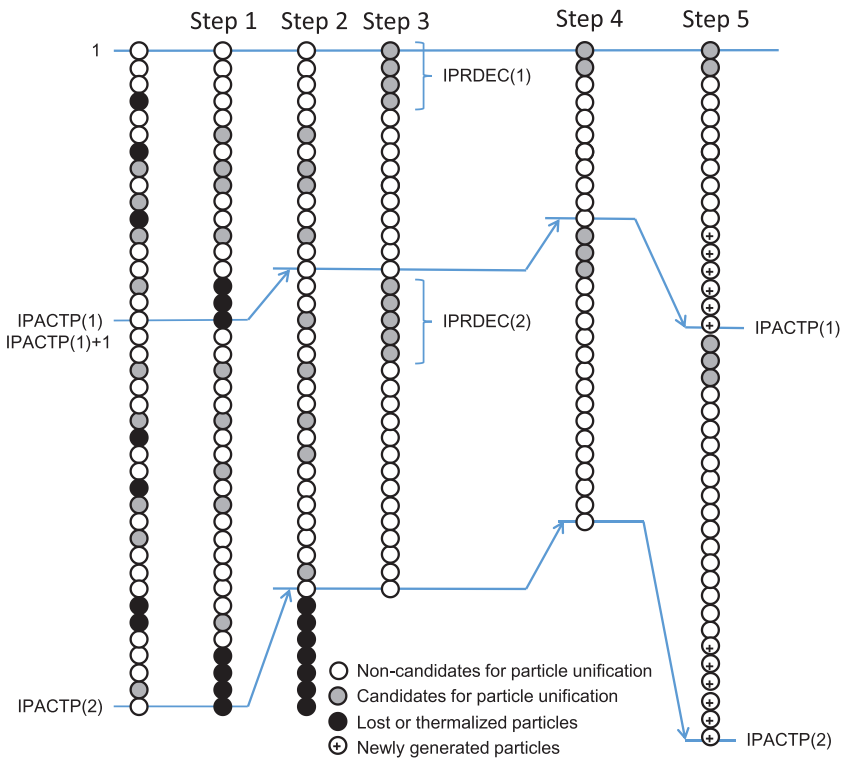

Figure 3. The rearrangement of test particles in the non-steady-state scheme.

generated test particles until they are lost to the wall or slow down, the main loop in the NSS scheme is repeatedly executed for every Δt_{NSS}. At the end of each NSS loop, the plasma parameters, the NBI conditions and the 3D-magnetic fields are updated for the next NSS step. Using these new parameters, new fast-ion test particles are generated and added to those remaining from the previous step. Thus, the number of test particles is increased step by step in the NSS scheme. In order to avoid a substantial increase in the amount of CPU time required due to this increase in the number of test particles, the NSS OFMC code employs a numerical technique to reduce the number of test particles by particle pairing and unification while maintaining the physical quantities of the fast ions, as described in section 2.2.2.

Prior to the calculations which reduce the number of particles, all test particles are rearranged to eliminate loss particles and to identify candidates for unification.

2.2.1. Particle rearrangement. The procedure to achieve particle rearrangement is schematically shown in figure 3. The OFMC code can handle two kinds of fast ions, NBI produced fast ions and fusion products. In figure 3, IPACTP(1) indicates the number of NBI-produced fast ions (the first kind) and IPACTP(2), the total number of fast ions (which include the second kind). In the first and second steps, lost or thermalized particles are moved to the tail end and eliminated from among the test particles. At the third step, particles which are candidates for particle unification are moved to the head. How to identify these candidates is described in the next subsection. The total numbers of candidates among the first and the second kinds of test particles are described by IPRDEC(1) and IPRDEC(2), respectively. At the point in time when IPACTP(1) or IPACTP(2) exceeds the number IPCONT which is specified in the input data, the process of particle pairing, unification and reduction shown in step 4 in figure 3 is switched on, as described in the next subsection.

After the process of particle pairing, unification and reduction, new fast ions are generated and added to the tail end of each kind of test particles at step 5. The details of the process of particle pairing and unification are described in the next subsection.

2.2.2. Reduction in the number of test-particles through pairing and unification. A reduction in the number of test particles is achieved by pairing similar particles in the phase space and unifying the pairs into one while maintaining their physical quantities.

There are three basic parameters to characterize a guiding-center orbit in an axi-symmetric field; the particle energy E, the magnetic moment μ and the canonical angular momentum P_ϕ. Here, we define these parameters as follows:

$$E = \frac{1}{2} m_{\mathrm{f}} (v_\perp^2 + v_{//}^2), \tag{6}$$

$$P_\phi = \Psi - \frac{m_{\mathrm{f}}}{e_{\mathrm{f}}} \frac{B_\phi}{B} R v_{//} \approx \Psi - \frac{m_{\mathrm{f}}}{e_{\mathrm{f}}} R v_{//}, \tag{7}$$

$$\mu = \frac{m_{\mathrm{f}} v_\perp^2}{2B} \approx \frac{m_{\mathrm{f}} R v_\perp^2}{2 R_t B_t}, \tag{8}$$

where m_{f} and e_{f} are the mass and the charge of fast ions, respectively; and B_t is the magnetic field at plasma center $R = R_t$. Since equations (6) and (8) give the major radius of the banana tip point as

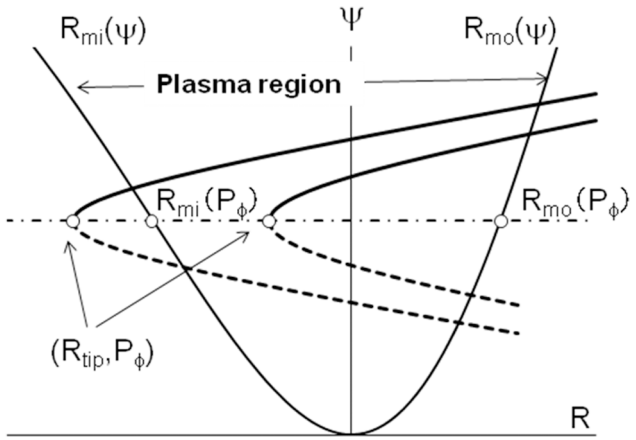

Figure 4. Schematics of fast-ion trajectories in (R, ψ) space.

$$R_{\rm tip} = \frac{R_t B_t \mu}{E}, \tag{9}$$

we employ $R_{\rm tip}$ instead of μ as one of the basic parameters. Each of these parameters is equally divided into small meshes and all the test particles are sorted using these parameters. Even if the above three parameters are close the orbit of particles with a positive velocity parallel to the magnetic field is different from that particles with a negative velocity. Therefore, particles are divided into two groups one with positive parallel velocities and another with negative velocities. The sorting is executed for the two groups separately. It is well known that significant radial transport occurs when the pitch-angle of a particle crosses the banana-transit boundary. Consequently, the pairing and unification should be made among banana or transit particles separately to avoid causing any numerical transport from the pairing and unification of two particles.

In order to meet this condition, a new parameter

$$\eta = \frac{R_{\rm tip}}{R_{\rm mi}(P_\phi)} \tag{10}$$

is employed, where $R_{\rm mi}(P_\phi)$ is the radial position of the magnetic surface on the mid-plane on the inner side of the torus at $\psi = P_\phi$, as shown in figure 4. The particles with $\eta > 1.0$ can be categorized as banana particles and those with $\eta < 1.0$ as transit. The sorting mesh size for η is given by $1.0/N_{\rm tip}$, where $N_{\rm tip}$ is input data.

The particle sorting to find possible pairings is executed with respect to the three parameters, E, P'_ϕ and η, where P'_ϕ is the canonical angular momentum normalized by the poloidal flux function at the plasma surface ψ_a, that is $P'_\phi = P_\phi/\psi_a$. Since $R_{\rm mi}$ changes non-linearly with ψ near the plasma center and particles near the plasma surface are apt to be lost, we apply the above particle sorting to those particles which are in the range

$$P'_{\phi-\min} < P'_\phi < P'_{\phi-\max}, \tag{11}$$

where $P'_{\phi-\min}$ and $P'_{\phi-\max}$ are the minimum and the maximum values of P'_ϕ given by input data and their default values are 0.1 and 0.8, respectively. Since most loss particles in a non-axi-symmetric field are banana particles, the NSS OFMC code has an option to exempt the banana particles from the particle sorting selected using input data.

If we find more than one particle in a (E, P'_ϕ, η) sorting box, particle pairings are made using a Monte-Carlo technique. We form as many pairs as possible from among all particles in the sorting box to reduce the number of particles. For each selected pair, four physical quantities of particle 1 and 2 are unified as follows:

$$w = w_1 + w_2, \tag{12}$$

$$E = \frac{E_1 w_1 + E_2 w_2}{w}, \tag{13}$$

$$\mu = \frac{\mu_1 w_1 + \mu_2 w_2}{w}, \tag{14}$$

$$P_\phi = \frac{P_{\phi 1} w_1 + P_{\phi 2} w_2}{w}, \tag{15}$$

where w is the particle weight which reflects the birth rate.

Using the above new parameters, the initial conditions of the unified particles are given by the following steps:

Step 1: The major radius position R is randomly given by a value between $R_{\rm tip}$ and $R_{\rm mo}(P_\phi)$ for a banana particle and a value between $R_{\rm mi}(P_\phi)$ and $R_{\rm mo}(P_\phi)$ for a transit particle, where $R_{\rm mo}(P_\phi)$ is the radial position of the magnetic surface on the mid-plane on the outer side of the torus at $\psi = P_\phi$ as shown in figure 4.

Step 2: With the above R and μ,

$$v_\perp = \sqrt{\frac{2R_t B_t \mu}{m_{\rm f} R}}. \tag{16}$$

Step 3: With the above $v_\perp$ and ,

$$v_{//} = \pm\sqrt{\frac{2}{m_{\rm f}}E - v_\perp^2} = \pm\sqrt{\frac{2E}{m_{\rm f}}}\sqrt{\frac{R - R_{\rm tip}}{R}} \tag{17}$$

Step 4: With the above $v_{//}$ and P_ϕ,

$$\psi = P_\phi \pm \frac{\sqrt{2m_{\rm f}E}}{e_{\rm f}}\sqrt{R(R - R_{\rm tip})}. \tag{18}$$

Step 5: With the above ψ and R, the vertical position Z is calculated using a 2D table of $Z(R, \psi)$

Step 6: The toroidal angle of the unified particle is given by a random number between 0 and 2π.

Note that the above procedure is basically for the guiding-center-orbit following scheme. In the gyro-orbit following scheme, prior to the above calculations of particle sorting, the guiding-center position $\vec{r}_{\rm gc} = (R, \phi, Z)$ and $(v_{//}, v_\perp)$ are calculated from the gyro-orbit position $\vec{r}_{\rm gy} = (R_{\rm gy}, \phi_{\rm gy}, Z_{\rm gy})$ and velocity $\vec{v}_{\rm gy} = (v_{R-{\rm gy}}, v_{\phi-{\rm gy}}, v_{Z-{\rm gy}})$ as follows:

$$\vec{r}_{\rm gc} = \vec{r}_{\rm gy} + \frac{m_{\rm f}}{e_{\rm f}B^2}\vec{v}_{\rm gy} \times \vec{B}, \tag{19}$$

$$v_{//} = \frac{1}{B}(B_R v_{R-{\rm gy}} + B_\phi v_{\phi-{\rm gy}} + B_Z v_{Z-{\rm gy}}), \tag{20}$$

$$v_\perp = \sqrt{\frac{2}{m_{\rm f}}E - v_{//}^2}, \tag{21}$$

where $\vec{B} = (B_R, B_\phi, B_Z)$ is the magnetic field at $\vec{r}_{\rm gy}$. After the calculations of the above particle sorting, pairing and unification, using $\vec{r}_{\rm gc} = (R, \phi, Z)$ and $(v_{//}, v_\perp)$, the gyro-orbit position $\vec{r}_{\rm gy} = (R_{\rm gy}, \phi_{\rm gy}, Z_{\rm gy})$ and velocity $\vec{v}_{\rm gy} = (v_{R-{\rm gy}}, v_{\phi-{\rm gy}}, v_{Z-{\rm gy}})$ are calculated with the unified $\vec{r}_{\rm gc} = (R, \phi, Z)$ and $(v_{//}, v_\perp)$ as follows:

$$\vec{r}_{\rm gy} = \vec{r}_{\rm gc} - \frac{m_{\rm f}}{e_{\rm f}B^2}\vec{v}_{\rm gy} \times \vec{B}, \tag{22}$$

$$v_{R-{\rm gy}} = v_\perp \frac{b_\phi}{\sqrt{1-b_Z^2}}\cos\xi - v_\perp \frac{b_R b_Z}{\sqrt{1-b_Z^2}}\sin\xi + v_{//} b_R, \tag{23.1}$$

$$v_{\phi-{\rm gy}} = -v_\perp \frac{b_R}{\sqrt{1-b_Z^2}}\cos\xi - v_\perp \frac{b_\phi b_Z}{\sqrt{1-b_Z^2}}\sin\xi + v_{//} b_\phi, \tag{23.2}$$

$$v_{Z-{\rm gy}} = v_\perp \sqrt{1-b_Z^2}\sin\xi + v_{//} b_Z, \tag{23.3}$$

where ξ is a random number between 0 and 2π, $b_R = B_R/B$, $b_\phi = B_\phi/B$ and $b_Z = B_Z/B$. The magnetic field in equations (22)–(23.3) is approximately given by the field at $\vec{r}_{\rm gc}$.

The new initial conditions of the unified particle, $\vec{r}_{\rm gc}$ and $(v_{//}, v_\perp)$ or $\vec{r}_{\rm gy}$ and $\vec{v}_{\rm gy}$, are replaced with those of the pair and the partner is removed from among the test particles.

2.2.3. Calculations of fast-ion relevant physical quantities. In the non-steady-state scheme, the fast-ion relevant physical quantities which correspond to those in the steady-state scheme as given by equations (4) and (5) are calculated at every $\Delta t_{\rm NSS}$ as follows:

$$P(\psi_i, T_{\rm NSS}(n)) = \int_{T_{\rm NSS}(n-1)}^{T_{\rm NSS}(n)} \sum_{k(i)} p(\psi_k(t)) w_k {\rm d}t, \tag{24}$$

$$P^\beta_{\rm dep}(\psi_i, T_{\rm NSS}(n)) = -\sum_{m=M_{\rm NSS}(n-1)}^{M_{\rm NSS}(n)} \sum_{k(i)} \Delta E^\beta(\psi_k(t_m)) w_k, \tag{25}$$

where $T_{\rm NSS}(n) = n\Delta t_{\rm NSS}$ and $M_{\rm NSS}(n) = nM_{\rm max}/N_{\rm NSS}$.

When D neutral beams are injected into a D plasma, for a 4D discretization with respect to $(R, Z, v, v_{//}/v)$ and $p = 1.0$ in equation (24), the 4D distribution of D fast-ion density at non-steady-state time node $T_{\rm NSS}(n)$, $n_{\rm D}^{\rm f}(R, Z, v, v_{//}/v, T_{\rm NSS}(n))$ can be estimated. If we employ fusion produced tritons as the second test particle species, the birth rate of tritons produced by D-beam and D-thermal fusion reactions w_k can be calculated using $n_{\rm D}^{\rm f}(R, Z, v, v_{//}/v, T_{\rm NSS}(n))$ and the time dependent bulk D-ion density distribution. Through the calculations of orbit following and Coulomb collisions during the next $\Delta t_{\rm NSS}$, the total neutron rate for D–T reactions at $t = T_{\rm NSS}(n+1)$ is obtained as $\sum_i P(\psi_i, T_{\rm NSS}(n+1))$ with $p = n_{\rm D}\langle\sigma v\rangle_{\rm DT}$ in equation(24). As described in section 2.1, a two-step procedure is necessary for the calculations of tritons produced by fusion reactions between D-beams and D-plasma-ions in the steady-state scheme. Using the non-steady-state scheme, however, similar results can be obtained in a single step if we allow a small time delay for $\Delta t_{\rm NSS}$.

3. An application of the NSS-OFMC code

Recent experimental results show that Type I ELMs can be suppressed effectively by applying RMPs produced by external magnetic coils [6–8]. The application of RMPs, however, can cause additional fast-ion losses. The effects of RMPs on the confinement of NBI-produced fast ions in the MAST were investigated experimentally [15]. It was found that in single null-diverted (SND) MAST pulses with a relatively low plasma current (400 kA), the total neutron emission dropped by approximately a factor of two when RMPs with a toroidal mode number $n = 3$ were applied. The experimental results are shown in figure 4 of [15].

As part of the verification and validation of the NSS-OFMC code, calculations of the time dependent neutron rates were made with a focus on a typical MAST shot #30086 in which the above mentioned drop of neutron emissions was observed.

3.1. Simulation conditions

According to the experimental data of the shot, the following calculation parameters are assumed to be invariable in time;

- MHD equilibrium,
- Zeff,
- NBI parameters,
- Toroidal field (TF) ripple.

On the other hand, the following parameters are assumed to be variable;

- ELM mitigation RMP field,
- Plasma rotation velocity,
- Plasma density and temperature.

The MHD equilibrium of SND MAST shot #30086 is shown in figure 5. The major radius of the magnetic axis $R_{\rm t} = 1.055$ m, the toroidal magnetic field at the magnetic axis $B_{\rm t} = 0.386$ T and the plasma current $I_{\rm p} = 428$ kA. For reference, the radial distribution of the safety factor $q_{\rm s}$ is shown in figure 6.

In MAST, the TF coils are installed along the surface of the vacuum vessel and the poloidal field coils are installed inside the vessel. The inner and the outer bores of the TF coils are also shown in figure 5. There are 12 coils, each about 4 cm thick. Using the TF coil geometry, a vacuum TF ripple field, hereafter simply referred to as TFR, is calculated by the Biot–Savart method. Due to a restriction in using the OFMC code, we employed a virtual first wall, beyond which particles are presumed to be lost. The virtual wall is shown in figure 5 by a dashed line.

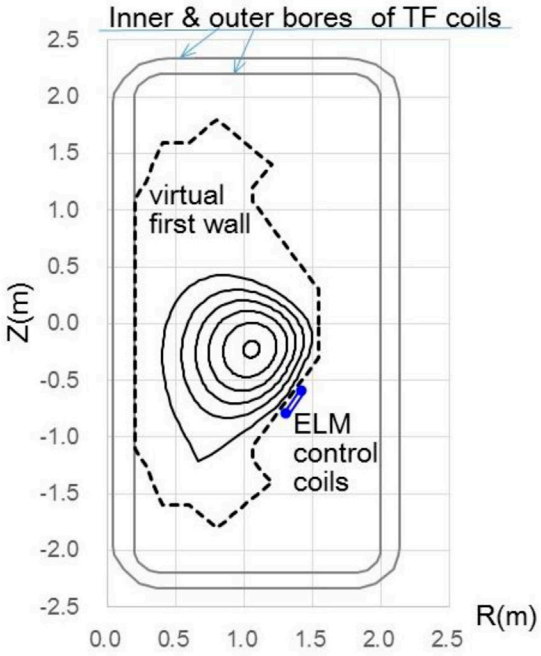

Figure 5. The 2D MHD equilibrium for MAST shot #30086 and the geometries of the virtual first wall, TF coils and ELM control coils.

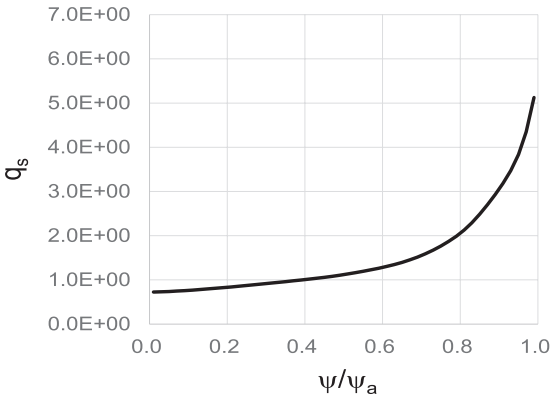

Figure 6. The radial distribution of the safety-factor.

MAST has two neutral-beam lines with primary injection energies in shot #30086 of $E_b = 71$ keV and 62 keV. Each beam is tangentially injected and contains neutral beams born at E_b, $E_b/2$ and $E_b/3$. The details of the two NB lines used in the present calculations are summarized in table 2.

The ELM control system to induce RMPs in MAST consists of 18 in-vessel coils (6 above the vacuum vessel midplane and 12 below the midplane) [20]. In the present work, we only used the lower set of coils, the poloidal position of which is also shown in figure 5. In shot #30086, RMPs with a toroidal mode number $n = 3$ were induced by alternately exciting only every other coil. The flat-top coil current $I_{\text{coil-top}}$ in shot #30086 is 4.0kAT. The 3D distribution of the flat-top RMP field is calculated by the Biot-Savart method in prior to the non-steady-state calculations.

The time variation of the RMP field is simply given by multiplying the flat-top field by a time-variation factor $f_{\text{coil}}(t)$ which is given by the ratio of the coil current at time t, $I_{\text{coil}}(t)$ to $I_{\text{coil-top}}$. The variation in f_{coil} is shown by the solid line in figure 7. In the present work, a vacuum RMP field is employed and the time delay due to the penetration of the field into the plasma is not taken into account. The variation in the plasma rotation velocity is also given by multiplying the rotation velocity at $t < 0.36$ s by a factor $f_{\text{rot}}(t)$. Taking the experimental data into account, the factor f_{rot} is assumed to be reduced after the application of the RMP field as shown by the dashed line in figure 7. Assuming that the poloidal rotation is much slower than the toroidal, the rotation velocity parallel to the magnetic field line is approximately given by the toroidal rotation velocity.

Table 2. NBI lines used in MAST shot #30086.

NBI Line	#1	#2
Primary injection energy E_b (keV)	71	62
Beam components (power ratio) P(E_b): P(E_b/2): P(E_b/3)	88.7: 9.7: 1.6	72.1: 26.4: 1.5
Total power (MW)	2.053	1.515

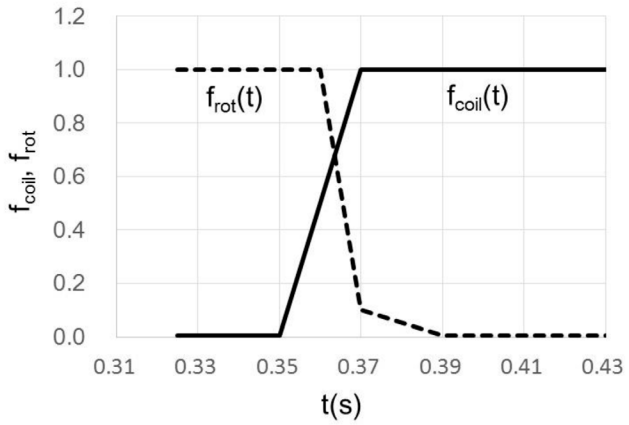

Figure 7. Time-variation factors for the RMP field f_{coil} and plasma rotation f_{rot}.

The radial distribution of plasma density, temperature and plasma rotation at time $t < 0.36$ s, $t = 0.37$ s and $t > 0.39$ s are shown in figures 8(A)–(C), respectively. The density and temperature profiles were measured using Thompson scattering, and the rotation profile was determined using impurity charge exchange. In the NSS-OFMC simulations, the profiles of these parameters at a point in time between the time nodes was modelled using linear interpolation of the measured profiles in time.

In the present work, charge-exchange and reionization processes were switched-off for simplicity of calculation. The neglect of these processes is likely to have led to a slight underestimate in the neutron rates computed using NSS-OFMC for MAST.

In the present calculations the following time meshes were employed;

$$\Delta t_{\text{orbit}} = 1 \times 10^{-2} \tau_{\text{gyro}} \text{ for the FO following,}$$

$$\approx 5 \times 10^{-3} \frac{R_{\text{mo}}}{v\sqrt{1 - R_{\text{tip}}/R_{\text{mo}}}} \text{ for the GC following,}$$

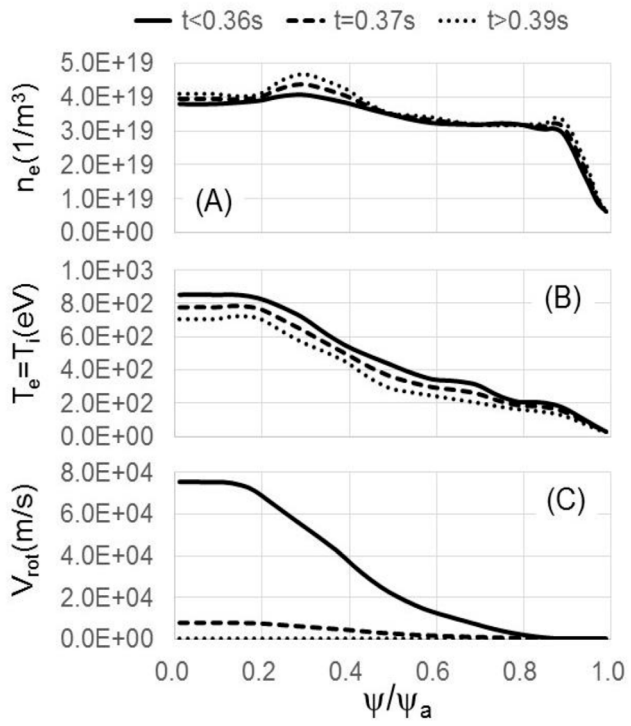

Figure 8. Radial profiles of plasma density (A), temperature (B) and plasma rotation (C) at time $t < 0.36$ s, $t = 0.37$ s and $t > 0.39$ s.

$$\Delta t_{\mathrm{col}} = 1 \times 10^{-6} \tau_{\mathrm{s0}},$$

where τ_{gyro} is the gyromotion period and R_{mo} is the radial position of the magnetic surface on the mid-plane on the outer side of the torus at $\psi = P_\phi$ (see figure 4). These parameters have been used in a benchmark test for the evaluation of fast-ion confinement in the ELM control field in MAST. The experimental results are briefly described in [15]. These parameters were commonly used in the NSS and the SS calculations. Concerning the NSS characteristic parameters used in the present calculations, the NSS time step was

$$\Delta t_{\mathrm{NSS}} = 1 \times 10^{-2} \tau_{\mathrm{s0}} \approx 7.8 \times 10^{-4} \mathrm{s},$$

the number of NBI test particles which are newly generated at every Δt_{NSS}

$$\Delta IP_{\mathrm{NBI}} = 240,$$

and the three numbers of the meshes N_{eng}, N_{pfai} and N_{tip} which give the size of the sorting box with respect to E, P'_ϕ and η (see section 2.2.2) were 20, 20 and 20, respectively.

3.2. Simulation results and discussions

Concerning the data analysis of neutron rates in such a low magnetic field as MAST shot #30086, a simple question arises as to whether there are any essential differences between the results using the GC-following and FO-following schemes. First of all, two non-steady-state calculations using the GC-following and FO-following schemes in an axi-symmetric field with plasma parameters as shown in figure 8 were made. The time variations in the neutron rates according to the former and the latter calculations are shown by the crosses and the open triangles in figure 9, respectively. The experimental data is also shown by the solid curve in figure 9. As shown in figure 9, the GC-following scheme overestimates the neutron rates.

In order to clarify the reason for the variation in these estimates, the power losses of fast ions are compared. The results are shown in figure 10. The thick curves show the results for FO following with plasma rotation and the thin curves without rotation. The upper two curves are the results with the RMPs and the TF ripple and the lower three curves are those in the axi-symmetric field. The results from the GC-following scheme which correspond to the crosses in figure 9 showing the estimates of the neutron rate are shown by the dotted curve in figure 10. Comparing the results of the lower thick curve with those of the dotted curve, the power loss obtained by the GC-following scheme is somewhat smaller than that obtained by FO-following. This indicates that the GC following might be useful for a rough estimation of fast-ion losses in MAST. This also indicates that the difference between the two losses is too small to account for the differences in the neutron rates as shown in figure 9. There might be another reason for the difference in the neutron rates. In order to identify the reason for this difference, we have examined a typical full orbit without Coulomb collisions.

The thin solid curve in figure 11(A) shows the one bounce full-orbit motion of a D fast ion born at $(R, \phi, Z) = (1.14\,\mathrm{m}, 0.0, -0.3\,\mathrm{m})$ with $E = 71$ keV and $v_{//}/v = 0.174$. For reference, the guiding center calculated from the full orbit using equation (19) is also shown in figure 11(A) by the thick solid curve. Note that the Larmor radius of fast ions is comparable to the plasma minor radius in MAST shot #30086. The neutron yield rates measured on the full orbit and at the guiding center are shown in figure 11(B) by the thin and thick solid curves, respectively. Since the beam energy is much larger than the plasma temperature, the D–D fusion reaction rate $\langle \sigma v \rangle_{\mathrm{DD}}$ is approximately given by the beam energy, and the neutron yield rate $n_{\mathrm{D}} \langle \sigma v \rangle_{\mathrm{DD}}$ is approximately proportional to the plasma density shown in figure 8(A). Consequently, if the Larmor radius of fast ions is comparable to the plasma minor radius, the neutron yield rate along the full orbit substantially changes as shown by the thin curve in figure 11(B). The neutron yield rate averaged over each gyro-period is shown by the thick dashed curve in figure 11(B). It is shown that the gyro-averaged neutron yield rate is substantially smaller than the neutron yield rate measured at the guiding center. In order to emphasize the finite Larmor radius (FLR) effects on the neutron yield in figure 11(B), we employed a banana particle. Generally, the Larmor radius of a transit particle is smaller than that of a banana particle. Though the FLR effects on the neutron yield rate for transit particles are somewhat smaller than those for banana particles, the FLR effects are common to all the fast ions in a low magnetic-field plasma with a non-linear distribution of neutron yield rate. The FLR effects on the neutron yield may be another reason for the differences in the neutron rates shown by the crosses and open circles in figure 9.

Note that the guiding center calculated from the full orbit is very bumpy as shown in figure 11(A). This implies that the GC following is no longer a good approximation in such a low magnetic field as MAST shot #30086. Hereafter, all calculations were made using the FO-following scheme.

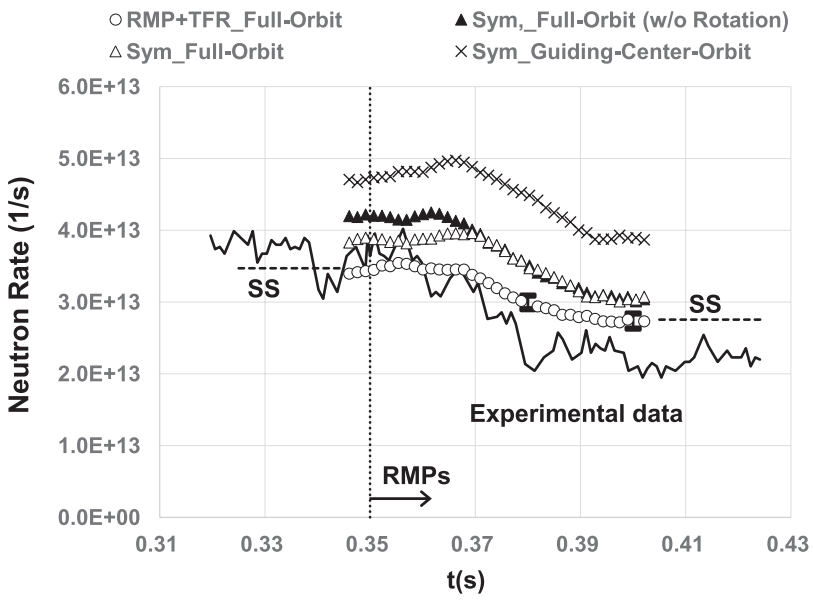

Figure 9. Neutron rates from the NSS calculations for MAST shot #30086. The neutron rates in an axi-symmetric field with plasma rotation using GC-following and FO-following schemes are shown by the crosses and open triangles, respectively. The neutron rate in an axi-symmetric field without plasma rotation using FO following is shown by the closed triangles. The neutron rate with the vacuum RMPs and TF ripples with plasma rotation using FO following is shown by the open circles with Monte-Carlo error bars at $t = 0.38$ and 0.4 s. The two horizontal dashed lines are the results from the steady-state (SS) calculations. The experimental data are shown by the solid curve.

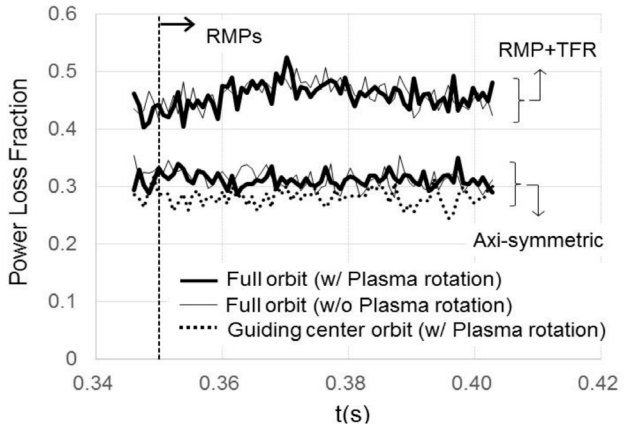

Figure 10. Power loss fractions with and without plasma rotation using the FO-following scheme are shown by the thick and thin solid curves, respectively. The upper two curves are the results with the RMPs and TF ripples; the lower three curves are those in the axi-symmetric field. The dotted curve is the power loss fraction with plasma rotation using the GC-following scheme.

In MAST shot #30086, as shown in figure 8(C), the plasma rotation velocity near the plasma center before the RMPs are applied, $t < 0.35$ s, amounts to about 3% of the injected D beam velocity. This may have a substantial effect on the slowing-down process of fast ions or the D–D fusion reaction rate. For the calculations of Coulomb collisions and the neutron rates, assuming that bulk plasma particles are Maxwellian, the particle velocities in the rest frame first are converted into those in the rotating frame. After calculating the Coulomb collisions and the neutron rates, the velocities are converted back into those in the rest frame (see equations (A.19)–(A.22)).

For comparison, calculations without plasma rotation were made. The variation of the neutron rate in the axi-symmetric field without the plasma rotation is shown by the closed triangles in figure 9. Figure 9 shows that the neutron rate before the start of RMPs is reduced by about 10% due to the plasma rotation in MAST shot #30086. For reference, the variations in the loss of fast ions with and without plasma rotation are shown in figure 10 by the thick and thin curves for both axi-symmetric and RMP+TFR fields. No significant differences between the losses with and without plasma rotation are found for both fields. This implies that the effect of plasma rotation on the slowing down process might be small.

Finally, the calculation results on the neutron rate in the RMP+TFR field and the experimental results are shown in figure 9 by the open circles and the solid curves, respectively. The calculation results approximately agree with the experimental data.

The differences between the neutron rates shown by the open triangles and circles in figure 9 and the differences in power loss fractions between the upper and the lower curves in figure 10, can be attributed to the effect of TFR only at times before the start of RMPs ($t = 0.35$ s), and to the combined effect of the RMPs and TFR at later times. The effect of the TF ripple is significant for both neutron rates and fast-ion losses throughout the shot in MAST, and considerably greater than that found by McClements and Hole [21]. This is likely to be due mainly to the fact that the plasma current in the shot considered here (400 kA) was lower than that used in the modelling reported in [21] (726 kA), with the result that otherwise well-confined beam ions migrated to regions of higher R and hence higher ripple amplitude in the former case.

The calculation parameters before the start of RMPs ($t < 0.35$ s) and at the flat-top ($t > 0.38$ s) are constant. Consequently, if the non-steady-state (NSS) algorithm works well, all calculation results from the NSS calculations at these times should agree with those from the steady-state (SS) calculations. For comparison, using the parameters at these times,

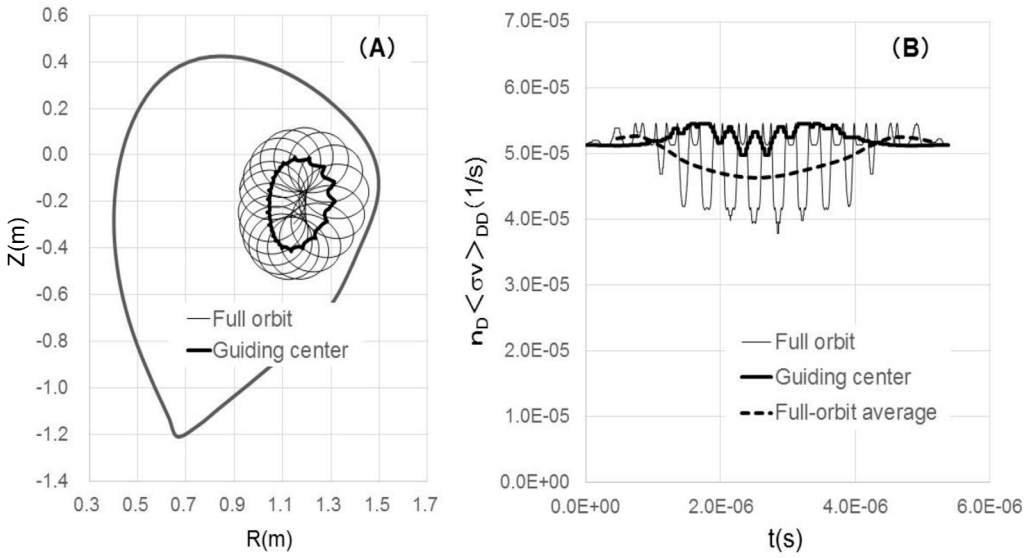

Figure 11. One bounce full-orbit motion of a D fast ion born at $(R, \phi, Z) = (1.14\,\mathrm{m}, 0.0, -0.3\,\mathrm{m})$ with $E = 71\,\mathrm{keV}$ and $v_{//}/v = 0.174$ is shown by the thin curve in (A). The guiding center calculated from the full orbit using equation (19) is shown by the thick curve in (A). The neutron yield rates measured along the full orbit and the guiding center are shown in (B) by the thin and thick solid curves, respectively. The neutron yield rate averaged over each gyro-period is also shown by the thick dashed curve in (B).

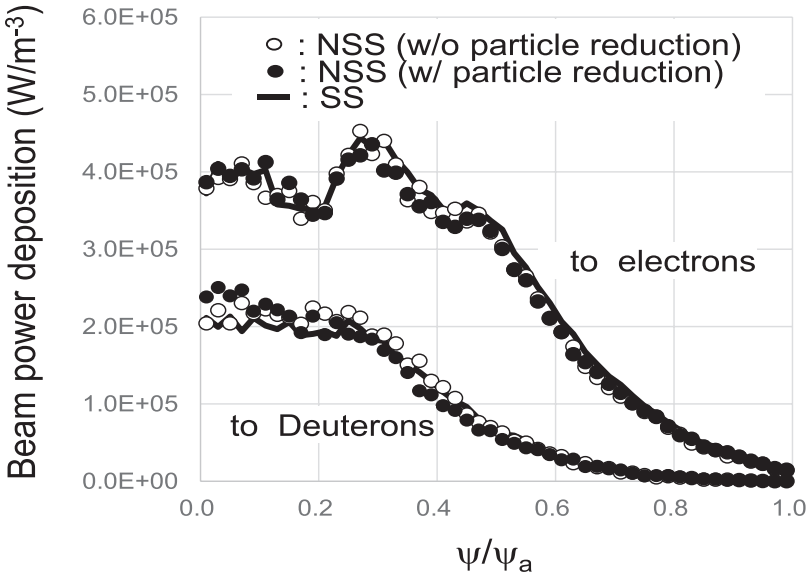

Figure 12. The radial profiles of the beam power deposited to the bulk electrons and deuterons at $t = 0.4\,\mathrm{s}$ obtained through the NSS calculations without the particle reduction are shown by the open circles; those through the NSS calculations with the particle reduction by the closed circles, respectively. The results from the SS calculations are shown by the solid curves.

steady-state FO-following calculations which correspond to the NSS calculations shown by the open circles in figure 9 were made. The results are also shown in figure 9 by the two horizontal dashed lines. NSS and SS calculation results agree very well. In a further comparison, the radial profiles of the beam power deposited to the bulk plasmas at $t = 0.4\,\mathrm{s}$ obtained through the NSS calculations and those through the SS calculations with parameters at $t > 0.38\,\mathrm{s}$ are shown in figure 12. The beam power deposited to bulk electrons and ions (D) from the NSS calculations which corresponds to the neutron rates shown by the open circles in figure 9 are shown by the open circles; those from the SS calculations by the solid curves, respectively. As mentioned below, the particle reduction step described in section 2.2.2 was not executed in the above NSS calculations due to the large number of loss particles. Figure 12 shows that results from the NSS and the SS calculations agree very well, which indicates the NSS algorithm works well and the calculation parameters are properly set.

Using the NSS OFMC code, the radial beam deposition profiles as shown in figure 12 can be calculated second by second taking into account the time dependent plasma parameters, beam conditions and 3D magnetic fields. If the NSS-OFMC code were directly coupled to a transport code, higher level data analyses including the time-variation of plasma parameters due to the loss of fast ions evaluated by the first principle method would be available. The biggest issue in pursuing this course is

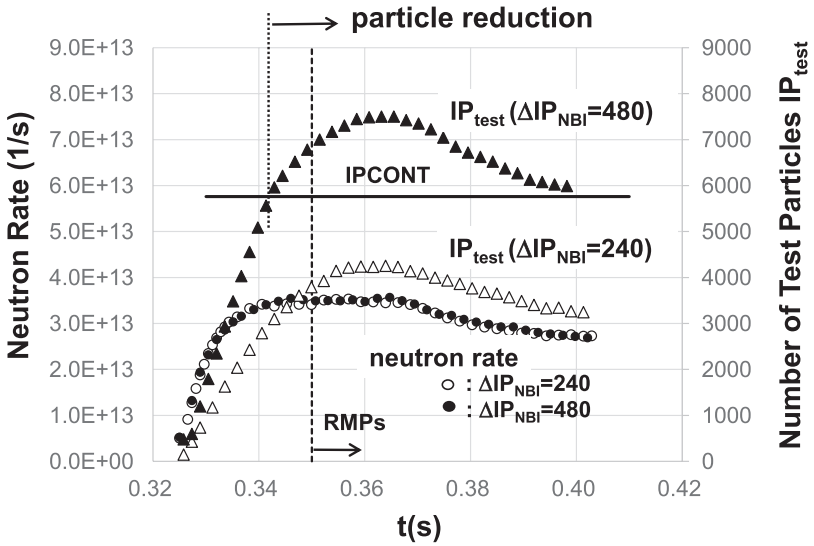

Figure 13. Time variations in the number of test particles and the neutron rate for $\Delta IP_{\mathrm{NBI}} = 240$ and 480 in the case of RMPs and TF-ripples. IPCONT is shown by the solid line.

the very long computational time required, as described below. To speed up the NSS calculations, new techniques, involving for example the use of general purpose graphical processing units (GPGPUs), could be used in the near future.

Note that there still remains a substantial difference between the simulation results in the 3D field of RMP+TFR and the experimental data, especially at the flat-top time when $t > 0.38$ s. Recent studies on the RMPs in MAST show that they are substantially modified by the plasma response [22]. The remaining discrepancy between the measured and modelled neutron rates after $t = 0.38$ s is likely to be due at least partly to the modification of RMPs by the plasma response.

In a typical case, the time variations in the number of test particles (triangles) and the neutron rate (circles) in the case of RMPs and TF-ripples are shown in figure 13. For all present NSS calculations, OFMC calculations were started at $t = 0.325$ s so that the neutron rates reached the steady-state level before the start of RMPs ($t = 0.35$ s) and 240 NBI test particles were generated at every Δt_{NSS}, that is, $\Delta IP_{\mathrm{NBI}} = 240$. It should be noted that the loss of fast ions in the shot #30086 is very large as described above. The number of loss particles due to the effects of the large Larmor radius, RMPs and thermalization are approximately balanced with or exceeds the number of test particles newly added, and consequently the number of test particles was kept within the number to switch on the calculations of particle reduction IPCONT (set to 5760) in all cases shown in figure 9.

In order to check the algorithm to reduce the number of test-particle described in section 2.2.2, we executed the NSS calculations increasing ΔIP_{NBI} from 240 to 480 so that the number of test particles exceeded IPCONT during the calculation, thereby triggering the particle reduction step. As shown in figure 13, the neutron rates with and without the particle reduction agree very well. The beam deposition profiles were also checked. The results are shown in figure 12. The beam deposition profiles with and without the particle reduction also generally agree well, Minor local differences which might be due to the Monte-Carlo error. A further check should be carefully made using more test particles and in a system with a better confinement of fast ions.

Table 3. CPU time for the calculations shown in figure 9.

Orbit-following scheme	Magnetic fields	Non-steady-state calculations (h)	Steady-state calculations (h)
Guiding-center orbit	Axi-symmetric	~0.8	
Full orbit	Axi-symmetric	~2.8	
	RMP+TFR	~15.5	~5.8

Each result shown in figure 9 was obtained as an average of 5 runs with a different random number series. Depending on the case and time, about 4000–5000 test particles were used for each run. For reference, the Monte-Carlo error bars describing the maximum and the minimum neutron rates in the vacuum RMPs and TF ripples with plasma rotation shown by the open circles in figure 9 are also shown at $t = 0.38$ and 0.4 s. Both errors are about $\pm 3.0\%$.

Lastly, the CPU times for the calculations shown in figure 9 using 8 cores of a Xenon(R) processor E7-4850, the performance of which is equivalent to 64GFLOPS, are summarized in table 3. As expected, the CPU time depends on the calculation conditions. The non-steady-state full-orbit following calculation shown in figure 9 took a CPU time which was 2–3 times longer than that of the steady-state calculation. Judging from the output of the non-steady-state calculations, this increase in the CPU cost might be acceptable.

4. Conclusions

A non-steady-state orbit-following Monte-Carlo algorithm has been developed as a new option of the OFMC code at JAEA. As part of the verification and validation of the new option, calculations of time dependent neutron rates were made for a specific MAST shot #30086 using vacuum RMPs and TF ripples. Results indicate that our calculations

approximately agree with the experimental data. In shot #30086, the magnetic field is so low that the Larmor radius of fast ions is a substantial fraction of the plasma minor radius and the neutron yield rate substantially changes along the gyro-trajectory. The resulting neutron yield rate averaged over each gyro-period becomes smaller than that at the guiding center. Therefore, the full-orbit following scheme should be employed for the estimation of neutron rates in MAST. The effect of plasma rotation on the neutron rate is important for MAST. The effects of both RMPs and TF ripples on fast-ion losses and on the neutron rate are also very important. In order to check the accuracy of computational modeling, we verified the algorithm to reduce the number of test-particles which is described in section 2.2.2. For a more precise treatment of the magnetic perturbations, the plasma response to these fields should be taken into account. Calculations of the neutron rate which take the plasma response into consideration will be made in the future.

Acknowledgments

Drs H Kamata, E Tada and R Yoshino are gratefully acknowledged for their continuous encouragement. This work was executed as part of a collaboration between the Tokyo Institute of Technology and the Japan Atomic Energy Agency (the National Institute for Quantum and Radiological Science and Technology from 1 April 2016). The development of the non-steady-state OFMC code was funded by the Japan Atomic Energy Agency. This work was part-funded by the RCUK Energy Programme (under grant EP/I501045) and the European Communities. The views and opinions expressed herein do not necessarily reflect those of the European Commission.

Appendix. Coulomb collision model used in the OFMC code

In the OFMC code, the effects of Coulomb collisions on the velocity changes of fast ions are simulated using the following Monte-Carlo techniques.

As shown in figure A1, if a fast ion undergoes longitudinal and transverse velocity changes $\Delta v_{\rm L}$ and $\Delta v_{\rm T}$ due to Coulomb collisions, the fast-ion velocities parallel and perpendicular to the magnetic field line on a guiding-center orbit are changed from $v_{//}$ and $v_{\perp}$ to

$$v_{//-\rm new} = v_{//} + \Delta v_{//}, \tag{A.1}$$

$$\Delta v_{//} = \Delta v_{\rm L}\frac{v_{//}}{v} + \Delta v_{\rm T}\frac{v_{\perp}}{v}\sin\Omega \tag{A.2}$$

and

$$v_{\perp-\rm new} = \sqrt{(v+\Delta v_{\rm L})^2 + \Delta v_{\rm T}^2 - (v_{//-\rm new})^2}, \tag{A.3}$$

respectively, where $v = \sqrt{v_{//}^2 + v_{\perp}^2}$ and Ω is the Larmor phase which is given by a random number. Using the new velocity

$$v_{\rm new} = \sqrt{v_{//-\rm new}^2 + v_{\perp-\rm new}^2}, \tag{A.4}$$

the energy change caused by the Coulomb collisions is given by

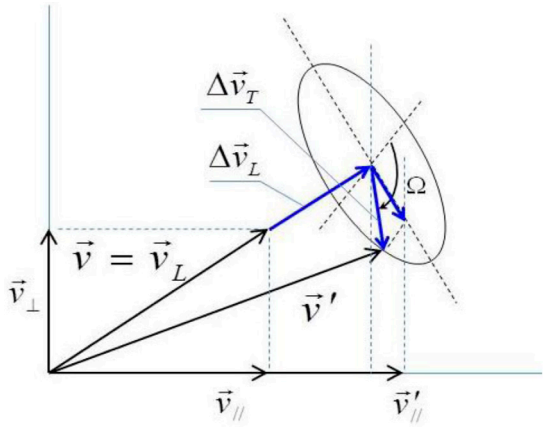

Figure A1. Schematics of Coulomb collision for a guiding-center orbit.

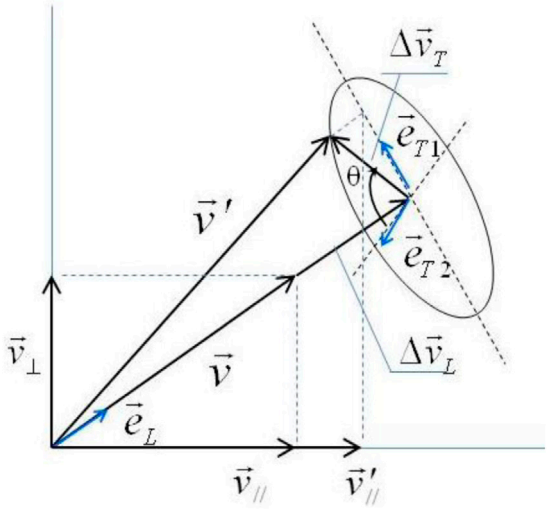

Figure A2. Schematics of Coulomb collision for a full orbit.

$$\begin{aligned}\Delta E &= \frac{1}{2}m_{\rm f}(v_{\rm new}^2 - v^2)\\ &= \frac{1}{2}m_{\rm f}(2v\Delta v_{\rm L} + \Delta v_{\rm L}^2 + \Delta v_{\rm T}^2)\\ &\approx m_{\rm f} v\Delta v_{\rm L}.\end{aligned} \tag{A.5}$$

In the full orbit following scheme, particle velocities are expressed as (v_R, v_ϕ, v_Z) in general cylindrical coordinate (R, ϕ, Z). The velocity change via Coulomb collisions is given by

$$\vec{v}_{\rm new} = \vec{v} + \Delta\vec{v}, \tag{A.6}$$

$$\Delta\vec{v} = \Delta v_R\vec{e}_R + \Delta v_\phi\vec{e}_\phi + \Delta v_Z\vec{e}_Z, \tag{A.7}$$

where $\vec{e}_R$, $\vec{e}_\phi$ and $\vec{e}_Z$ are the unit vectors along (R, ϕ, Z) directions and Δv_R, Δv_ϕ and Δv_Z are velocity changes along respective directions given by solving the following equations,

$$\left.\begin{aligned}&\Delta v_R a_1 + \Delta v_\phi b_1 + \Delta v_Z c_1 = \Delta v_{\rm L},\\ &\Delta v_R a_2 + \Delta v_\phi b_2 + \Delta v_Z c_2 = \Delta v_{\rm T}\sin\theta,\\ &\Delta v_R a_3 + \Delta v_\phi b_3 + \Delta v_Z c_3 = \Delta v_{\rm T}\cos\theta,\end{aligned}\right\} \tag{A.8}$$

where θ is the phase angle of $\Delta\vec{v}_{\rm T}$ as shown in figure A2. (a_1, b_1, c_1), (a_2, b_2, c_2) and (a_3, b_3, c_3) are the coefficients of longitudinal unit vector and two transverse unit vectors which vertically cross each other as follows;

$$\left.\begin{aligned}\vec{e}_{\rm L} &= a_1\vec{e}_R + b_1\vec{e}_\phi + c_1\vec{e}_Z,\\ \vec{e}_{\rm T1} &= a_2\vec{e}_R + b_2\vec{e}_\phi + c_2\vec{e}_Z,\\ \vec{e}_{\rm T2} &= a_3\vec{e}_R + b_3\vec{e}_\phi + c_3\vec{e}_Z.\end{aligned}\right\}. \tag{A.9}$$

For simplicity of calculation, here we employ $\vec{e}_{\rm T1}$ parallel to the R–Z plane, namely $b_2 = 0$. With this condition,

$$a_1 = v_R/v,\ \ b_1 = v_\phi/v,\ \ c_1 = v_Z/v,$$

$$a_2 = v_Z/\sqrt{v_R^2 + v_Z^2},\ b_2 = 0,\ c_2 = -v_R/\sqrt{v_R^2 + v_Z^2},$$

$$a_3 = a_1b_1/\sqrt{1 - b_1^2},\ b_3 = -\sqrt{1 - b_1^2},\ c_3 = b_1c_1/\sqrt{1 - b_1^2}.$$

Using the above coefficients, the solutions of equation (A.7) are given as

$$\left.\begin{aligned}\Delta v_R &= b_3c_2\Delta v_{\rm L} + (b_1c_3 - b_3c_1)\Delta v_{\rm T}\sin\theta - b_1c_2\Delta v_{\rm L}\cos\theta,\\ \Delta v_Z &= (\Delta v_{\rm T}\sin\theta - a_2\Delta v_R)/c_2,\\ \Delta v_\phi &= (\Delta v_{\rm T}\cos\theta - a_3\Delta v_R - c_3\Delta v_Z)/b_3.\end{aligned}\right\} \tag{A.10}$$

With these velocity changes, the new velocity is given by

$$v_{\rm new} = \sqrt{v_{R-\rm new}^2 + v_{\phi-\rm new}^2 + v_{Z-\rm new}^2}, \tag{A.11}$$

where

$$\left.\begin{aligned}v_{R-\rm new} &= v_R + \Delta v_R,\\ v_{\phi-\rm new} &= v_\phi + \Delta v_\phi,\\ v_{Z-\rm new} &= v_Z + \Delta v_Z.\end{aligned}\right\}. \tag{A.12}$$

As in the case of the guiding-center orbit following scheme, the energy change in the full orbit scheme is approximately given as

$$\Delta E \approx m_{\rm f}(v_R\Delta v_R + v_\phi\Delta v_\phi + v_Z\Delta v_Z). \tag{A.13}$$

In the OFMC code, time is normalized by the slowing down time of fast ions given by Coulomb collisions with plasma electrons at plasma center $\tau_{\rm s0}^{\rm f/e}$ (hereafter simply referred to as τ_{s0}) and all the velocities are normalized by the fast-ion velocity corresponding to the energy of the electron temperature at the plasma center $v_0 = \sqrt{2T_{\rm e0}/m_{\rm f}}$ where $m_{\rm f}$ is the mass of fast ions. Hereafter, all the velocities and time are normalized by v_0 and $\tau_{\rm s0}$, respectively, and are represented with primes. The longitudinal and transverse velocity change $\Delta v_{\rm L}'^{\beta}$ and $\Delta v_{\rm T}'^{\beta}$ caused by Coulomb collisions with Maxwellian field particles during a very small time interval $\Delta t'_{\rm col}(\approx 10^{-6})$ are given by respective normal random numbers with the following respective mean values and standard deviations [23];

$$\Delta\left\langle v_{\rm L}'\right\rangle^{\beta} = \Delta t'_{\rm col}\frac{3\sqrt{\pi}}{2}M_{\rm f}A_\beta^2\frac{m_\beta}{m_{\rm f}}\left(1 + \frac{m_{\rm f}}{m_\beta}\right)\frac{n_\beta}{n_{\rm e0}}\frac{T_{\rm e0}}{T_\beta}\frac{\varpi(\chi_\beta)}{2\chi_\beta}, \tag{A.14.1}$$

$$\Delta\left\langle v_{\rm L}'^{\,2}\right\rangle^{\beta} = \Delta t'_{\rm col}\frac{3\sqrt{\pi}}{2}M_{\rm f}A_\beta^2\sqrt{\frac{m_\beta}{m_{\rm f}}}\frac{n_\beta}{n_{\rm e0}}\sqrt{\frac{T_{\rm e0}}{T_\beta}}\frac{\varpi(\chi_\beta)}{2\chi_\beta^{3/2}}, \tag{A.14.2}$$

$$\Delta\left\langle v_{\rm T}'\right\rangle^{\beta} = 0, \tag{A.14.3}$$

$$\Delta\langle v_{\rm T}'^{\,2}\rangle^{\beta} = \Delta t'_{\rm col}\frac{3\sqrt{\pi}}{2}M_{\rm f}A_\beta^2\sqrt{\frac{m_\beta}{m_{\rm f}}}\frac{n_\beta}{n_{\rm e0}}\sqrt{\frac{T_{\rm e0}}{T_\beta}} \times\left(\varpi(\chi_\beta) + \frac{{\rm d}\varpi(\chi_\beta)}{{\rm d}\chi_\beta} - \frac{\varpi(\chi_\beta)}{2\chi_\beta}\right)\frac{1}{\chi_\beta^{1/2}}, \tag{A.14.4}$$

where

$$M_{\rm f} = \frac{(m_{\rm f}/m_{\rm e})^{3/2}}{(1 + m_{\rm f}/m_{\rm e})},$$

$$\chi_\beta = \frac{m_\beta v^2}{2T_\beta} = \frac{m_\beta}{m_{\rm f}}\frac{T_{\rm e0}}{T_\beta}v'^2,$$

$$\varpi(\chi_\beta) = {\rm Erf}(\sqrt{\chi_\beta}) - 2\sqrt{\frac{\chi_\beta}{\pi}}\exp(-\chi_\beta),$$

and β denotes field-particle species including impurities. The plasma parameters n_β and T_β in the above expressions are the functions of the normalized poloidal flux function ψ.

In a multi-species plasma, calculations of equations (A.1)–(A.5) for the guiding-center orbit scheme and (A.6)–(A.12) for the full orbit scheme are executed repeatedly for all the species β substituting $\Delta v_{\rm L}^{\beta}(= v_0\Delta v_{\rm L}'^{\beta})$ and $\Delta v_{\rm T}^{\beta}(= v_0\Delta v_{\rm T}'^{\beta})$ for $\Delta v_{\rm L}$ and $\Delta v_{\rm T}$. In the above calculations, the particle velocities are updated at each β step, that is,

$$v_{//} = v_{//-\rm new},$$

$$v_\perp = v_{\perp-\rm new},$$

in the guiding-center-orbit-following scheme and

$$v_R = v_{R-\rm new},$$

$$v_\phi = v_{\phi-\rm new},$$

$$v_Z = v_{Z-\rm new},$$

in the full-orbit-following scheme.

The energy change of fast ions due to Coulomb collisions with plasma-species β is also given by

$$\Delta E^{\beta} \approx 2T_{\rm e0}v'\Delta v_{\rm L}'^{\beta} \tag{A.15}$$

in the guiding-center-orbit-following scheme and

$$\Delta E^{\beta} \approx 2T_{\rm e0}(v_R'\Delta v_R' + v_\phi'\Delta v_\phi' + v_Z'\Delta v_Z') \tag{A.16}$$

in the full-orbit-following scheme.

The change in velocity parallel to the magnetic field line due to Coulomb collisions with plasma-species β is also given by

$$\Delta v_{//}^{\beta} = v_0\left(\Delta v_{\rm L}'^{\beta}\frac{v_{//}}{v} + \Delta v_{\rm T}'^{\beta}\frac{v_\perp}{v}\sin\Omega\right). \tag{A.17}$$

This expression is common to both guiding-center and full-orbit following schemes.

In a plasma rotating along the magnetic field line at

$$v_{//\mathrm{rot}} = \frac{B_\phi}{B} v_\phi + \frac{B_\mathrm{p}}{B} v_\mathrm{p}, \tag{A.18}$$

where v_ϕ and v_p are the toroidal and poloidal rotation velocities, respectively; and B_ϕ and B_p are the toroidal and ploloidal magnetic fields, respectively, the above calculations are executed as follows:

In the case of a guiding-center orbit following scheme, the fast ion velocities parallel and perpendicular to the magnetic field line in the rest frame are converted into those in the rotating frame as

$$\left.\begin{aligned} v_{//} &= v_{//} - v_{//\mathrm{rot}}, \\ v_\perp &= v_\perp. \end{aligned}\right\}. \tag{A.19}$$

After applying the above collisional calculations, the new velocities are converted back to those in the rest frame as

$$\left.\begin{aligned} v_{//-\mathrm{new}} &= v_{//-\mathrm{new}} + v_{//\mathrm{rot}}, \\ v_{\perp-\mathrm{new}} &= v_{\perp-\mathrm{new}}. \end{aligned}\right\}. \tag{A.20}$$

In the case of a full-orbit following scheme, the velocities (v_R, v_ϕ, v_Z) are converted into those in the rotating frame as

$$\left.\begin{aligned} v_R &= v_R - v_{//\mathrm{rot}} \frac{B_R}{B}, \\ v_\phi &= v_\phi - v_{//\mathrm{rot}} \frac{B_\phi}{B}, \\ v_Z &= v_Z - v_{//\mathrm{rot}} \frac{B_Z}{B}. \end{aligned}\right\}. \tag{A.21}$$

After applying the above collisional calculations, the new velocities are converted back to those in the rest frame as

$$\left.\begin{aligned} v_{R-\mathrm{new}} &= v_{R-\mathrm{new}} + v_{//\mathrm{rot}} \frac{B_R}{B}, \\ v_{\phi-\mathrm{new}} &= v_{\phi-\mathrm{new}} + v_{//\mathrm{rot}} \frac{B_\phi}{B}, \\ v_{Z-\mathrm{new}} &= v_{Z-\mathrm{new}} + v_{//\mathrm{rot}} \frac{B_Z}{B}. \end{aligned}\right\}. \tag{A.22}$$

References

[1] Tani K, Azumi M, Kishimoto H and Tamura S 1981 *J. Phys. Soc. Japan* **50** 1726
[2] White R B and Chance M S 1984 *Phys. Fluids* B **27** 2455
[3] Kurki-Suonio T *et al* 2009 *Nucl. Fusion* **49** 095001
[4] Akers R J *et al* 2012 *Proc. 39th EPS Conf. on Plasma Physics* P5.088
[5] Kramer G J, Budny R V, Bortolon A, Fredrickson E D, Fu G Y, Heidbrink W W, Nazikian R, Valeo E and Van Zeeland M A 2013 *Plasma Phys. Control. Fusion* **55** 025013
[6] Garcia-Munoz M *et al* 2013 *Plasma Phys. Control. Fusion* **55** 124014
[7] Garcia-Munoz M *et al* 2013 *Nucl. Fusion* **53** 123008
[8] Van Zeeland M A *et al* 2014 *Plasma Phys. Control. Fusion* **56** 015009
[9] Shinohara K *et al* 2011 *Nucl. Fusion* **51** 063028
[10] Tani K, Shinohara K, Oikawa T, Tsutsui H, Miyamoto S, Kusama Y and Sugie T 2012 *Nucl. Fusion* **52** 013012
[11] Oikawa T *et al* 2012 *Proc. 24th IAEA Fusion Energy Conf. (San Diego)* ITR/P1-35
[12] Koskela T, Asunta O, Hirvijoki E, Kurki-Suonio T and Äkäslompolo S 2012 *Plasma Phys. Control. Fusion* **54** 105008
[13] Goldston R J, McCune D C, Towner H, Davis S L, Hawryluk R J and Schmdt G L 1981 *J. Comput. Phys.* **43** 61
[14] Pankin A *et al* 2004 *Phys. Commun.* **159** 157–84
[15] McClements K G *et al* 2015 *Plasma Phys. Control. Fusion* **57** 075003
[16] Tani K, Takizuka T, Azumi M and Kishimoto H 1983 *Nucl. Fusion* **23** 657
[17] Tani K, Azumi M and Devoto R S 1992 *J. Comput. Phys.* **98** 332
[18] Tani K and Azumi M 2008 *Nucl. Fusion* **48** 085001
[19] Honda M, Takizuka T, Tobita K, Matsunaga G and Fukuyama A 2011 *Nucl. Fusion* **51** 073018
[20] Chapman I T *et al* 2012 *Plasma Phys. Control. Fusion* **54** 105013
[21] McClements K G and Hole M J 2012 *Phys. Plasmas* **19** 072514
[22] Liu Y Q, Gribov Y, Gryaznevich M P, Hender T C, Kirk A and Nardon E 2011 *Nucl. Fusion* **51** 083002
[23] Turbnikov B A 1965 *Rev. Plasma Phys.* **1** 105